

UC Davis

UC Davis Previously Published Works

Title

Correlation between structural phase transition and surface chemical properties of thin film SrRuO₃/SrTiO₃ (001)

Permalink

<https://escholarship.org/uc/item/49h2919k>

Journal

The Journal of Chemical Physics, 152(3)

ISSN

0021-9606

Authors

Kim, Dongwoo
Lim, Hojoon
Ha, Sung Soo
[et al.](#)

Publication Date

2020-01-21

DOI



10.1063/1.5134653

Peer reviewed

Correlation between structural phase transition and surface chemical properties of thin film SrRuO₃/SrTiO₃ (001) F

Cite as: J. Chem. Phys. **152**, 034704 (2020); <https://doi.org/10.1063/1.5134653>

Submitted: 31 October 2019 . Accepted: 23 December 2019 . Published Online: 16 January 2020

Dongwoo Kim, Hojoon Lim,  Sung Soo Ha, Okkyun Seo, Sung Su Lee, Jinwoo Kim, Ki-jeong Kim, Lucia Perez Ramirez, Jean-Jacques Gallet, Fabrice Bournel, Ji Young Jo, Slavomir Nemsak, Do Young Noh, and  Bongjin Simon Mun

COLLECTIONS

Paper published as part of the special topic on [Oxide Chemistry and CatalysisOXIDE2020](#)

F This paper was selected as Featured



View Online



Export Citation



CrossMark

ARTICLES YOU MAY BE INTERESTED IN

[Thickness-dependent orbital hybridization in ultrathin SrRuO₃ epitaxial films](#)

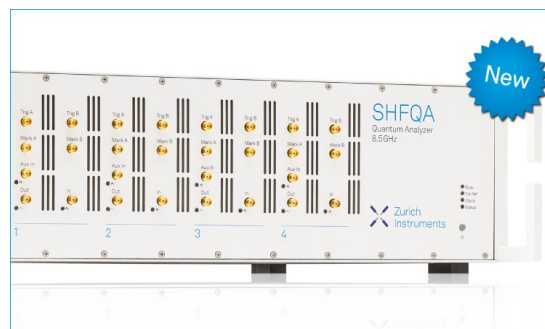
Applied Physics Letters **115**, 092906 (2019); <https://doi.org/10.1063/1.5110644>

[Epitaxial strain effect in tetragonal SrRuO₃ thin films](#)

Journal of Applied Physics **113**, 173912 (2013); <https://doi.org/10.1063/1.4803869>

[Metal-insulator transition in \(111\) SrRuO₃ ultrathin films](#)

APL Materials **7**, 091106 (2019); <https://doi.org/10.1063/1.5109374>



Your Qubits. Measured.

Meet the next generation of quantum analyzers

- Readout for up to 64 qubits
- Operation at up to 8.5 GHz, mixer-calibration-free
- Signal optimization with minimal latency

Find out more



Correlation between structural phase transition and surface chemical properties of thin film SrRuO₃/SrTiO₃ (001)

Cite as: J. Chem. Phys. 152, 034704 (2020); doi: 10.1063/1.5134653

Submitted: 31 October 2019 • Accepted: 23 December 2019 •

Published Online: 16 January 2020





View Online



Export Citation



CrossMark

Dongwoo Kim,^{1,a)} Hojoon Lim,^{1,a)} Sung Soo Ha,²  Okkyun Seo,³ Sung Su Lee,² Jinwoo Kim,⁴ Ki-jeong Kim,⁴ Lucia Perez Ramirez,⁵ Jean-Jacques Gallet,^{5,6} Fabrice Bournel,^{5,6} Ji Young Jo,² Slavomir Nemsak,⁷ Do Young Noh,^{1,b)} and Bongjin Simon Mun^{1,b)} 

AFFILIATIONS

¹Department of Physics and Photon Science, Gwangju Institute of Science and Technology, Gwangju 61005, South Korea

²School of Materials Science and Engineering, Gwangju Institute of Science and Technology, Gwangju 61005, South Korea

³Synchrotron X-ray Station at SPring-8, Research Network and Facility Services Division, National Institute for Materials Science (NIMS), Kouto, Sayo, Hyogo 679-5148, Japan

⁴Pohang Accelerator Laboratory, POSTECH, 127 Jigok-ro, Nam-gu, Pohang-si, Gyeongsangbuk-do 37673, South Korea

⁵Sorbonne Université, CNRS, Laboratoire de Chimie Physique Matière et Rayonnement, UMR 7614, Campus Pierre et Marie Curie, 4 place Jussieu, 75252 Paris Cedex 05, France

⁶Synchrotron SOLEIL, L'Orme des Merisiers, Saint-Aubin, F-91192 Gif-sur-Yvette, France

⁷Advanced Light Source, Lawrence Berkeley National Laboratory, Berkeley, California 94720, USA

Note: This article is part of the JCP Special Topic on Oxide Chemistry and Catalysis.

^{a)}**Contributions:** D. Kim and H. Lim contributed equally to this work.

^{b)}**Authors to whom correspondence should be addressed:** bsmun@gist.ac.kr and dynoh@gist.ac.kr

ABSTRACT

The correlation between the structural phase transition (SPT) and oxygen vacancy in SrRuO₃ (SRO) thin films was investigated by *in situ* X-ray diffraction (XRD) and ambient pressure X-ray photoelectron spectroscopy (AP-XPS). *In situ* XRD shows that the SPT occurs from a monoclinic SRO phase to a tetragonal SRO phase near ~200 °C, regardless of the pressure environment. On the other hand, significant core level shifts in both the Ru and Sr photoemission spectra are found under ultrahigh vacuum, but not under the oxygen pressure environment. The directions and behavior of the core level shift of Ru and Sr are attributed to the formation of oxygen vacancy across the SPT temperature of SRO. The analysis of *in situ* XRD and AP-XPS results provides an evidence for the formation of metastable surface oxide possibly due to the migration of internal oxygen atoms across the SPT temperature, indicating the close relationship between oxygen vacancy and SPT in SRO thin films.

© 2020 Author(s). All article content, except where otherwise noted, is licensed under a Creative Commons Attribution (CC BY) license (<http://creativecommons.org/licenses/by/4.0/>). <https://doi.org/10.1063/1.5134653>

INTRODUCTION

Perovskite materials with the ABO₃ structure have been extensively investigated for future applications in memory devices, energy storage devices, and electrodes for water-splitting due to their rich electronic/magnetic properties, i.e., ferroelectricity, ferromagnetism,

superconductivity, etc.^{1–12} In the selection of ideal perovskite materials for such applications, it is necessary to identify key physical parameters that determine the characteristics of perovskites. Among the key parameters, structural properties are known to have very close relation with diverse electronic/magnetic properties of perovskites.¹³ In general, the structural factor in perovskites

is divided into 3 categories, (i) Jahn-Teller distortion (LaMnO_3),¹⁴ (ii) cation displacement (BaTiO_3 , PbTiO_3),¹⁵ and (iii) octahedral tilting (SrRuO_3 and $\text{La}_{1-x}\text{Sr}_x\text{MnO}_3$).^{13,16} Especially, the octahedral tilting, the most common structural factor among perovskites,¹⁷ influences strongly the physical properties such as ferroelectricity, magnetism, and charge ordering.^{18,19} In perovskites with octahedral tilting, the B cation occupies the center of the BO_6 octahedron, and the distorted 6 surrounding oxygen atoms maintain the periodicity and corner connectivity relative to one or more symmetric axes.²⁰

SrRuO_3 (SRO) is one of the representative perovskite materials, which shows the octahedral tilting.²¹ Due to the chemical/thermal stability as well as good conductivity, SRO has been a popular choice for electrode materials of functional oxide films.²² In addition, the exotic transport properties of SRO have attracted much interest in basic research, e.g., superconductivity, ferromagnetism, and topological hall effect.^{23–31} Previously, it is reported that bulk SRO shows a structural phase transition (SPT) from the orthorhombic to tetragonal phase at 547°C , and from the tetragonal to cubic phase at 677°C .³² Interestingly, when prepared as a thin film (~less than 40 nm thick), SRO makes the SPT from the monoclinic to tetragonal phase at 200°C , which is significantly lower than the bulk SRO.³³ Although a substrate-induced strain is pointed out as the cause of the low temperature SPT of the SRO thin film, the exact mechanism of the SPT has not been answered.^{33,34} Many fabrication factors are known to have effects on the onset of SPT of SRO thin films, which include film thickness,³⁴ oxygen partial pressure during film growth,³⁵ substrate strain,³⁶ and temperature.³³ Among these, oxygen partial pressure during film growth is closely related to the oxygen vacancy, i.e., lesser oxygen gas pressure during sample fabrication increases the oxygen vacancy in the film. Since oxygen vacancy can be considered as a defect state, the conductivity, optical transparency, and other important physical properties of films are closely related to the amount of oxygen vacancy.³⁵ Previously, it is reported that the existence of oxygen vacancy in the SRO thin film varies the orbital hybridization between Ru $4d$ and O $2p$, affecting the electronic structure and transport properties of thin films.^{37,38} It is also found that the formation of oxygen vacancy at the Sr-O plane is more energetically favorable than the Ru-O plane.³⁷ Apparently, the concentration of oxygen vacancy in oxide materials has become a critical adjusting parameter for engineering the desired properties.^{39,40}

To illustrate the SPT of the SRO thin films, two different structures of SRO thin films are shown in Fig. 1, a tetragonal SRO (T-SRO), and monoclinic SRO (M-SRO). As the oxygen vacancies are generated at the Sr-O planes in T-SRO, the SRO thin film exhibits a tetragonal structure owing to the increase in Ru-Ru repulsion that suppresses the octahedral tilting,⁴¹ as shown in Fig. 1(a). On the other hand, in the case of M-SRO, the concentration of the oxygen vacancy is low and octahedral tilting prevails with the tilting angle of $\sim 0.45^\circ$ due to a substrate induced strain, as shown in Fig. 1(b).

To understand the role of oxygen vacancy, substantial efforts have been devoted with diverse analytic techniques, e.g., positron annihilation lifetime spectroscopy⁴² and scanning transmission electron microscopy.⁴³ Unfortunately, due to their poor sensitivity of probing techniques and highly diluted contents, the direct observation of oxygen vacancy still remains as a great challenge and its

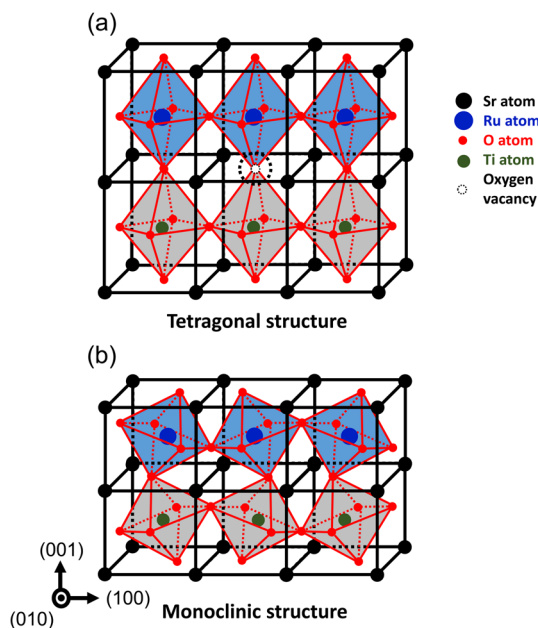


FIG. 1. Schematic view of (a) T-SRO and (b) M-SRO thin film, respectively. An oxygen vacancy in the Sr-O plane of T-SRO is energetically favorable.

role in transport properties of thin films is not well understood.^{44,45} In this report, we investigated the correlation between the SPT of the SRO thin film and oxygen vacancy with *in situ* X-ray diffraction (XRD) and ambient pressure X-ray photoelectron spectroscopy (AP-XPS). *In situ* XRD shows that the SPT occurs from M-SRO to T-SRO near $\sim 200^\circ\text{C}$, regardless of the pressure environment. When XPS is applied to monitor the surface chemical properties of the SRO film during the SPT temperature, Ru core level spectra shift toward the lower binding energy direction, whereas the Sr core level spectra move to the opposite direction under ultra-high vacuum (UHV) conditions. The directions of the core level shift of Ru and Sr can be interpreted with the formation of oxygen vacancy during the SPT of the SRO thin film. The features of valence band spectra of SRO thin films across the SPT temperature also reveal the evidence of oxygen vacancy formation. Then, when the oxygen vacancy is filled, the observed peak changes of XPS disappear. Combined analysis of *in situ* XRD and XPS results suggests that oxygen atoms migrated to the surface to form the surface oxide across the SPT temperature, revealing the close correlation between oxygen vacancy and SPT of SRO thin films.

EXPERIMENT

SRO thin films were epitaxially grown on TiO_2 terminated SrTiO_3 (STO) (001) substrates by pulsed laser deposition (PLD) with a KrF excimer laser ($\lambda = 248 \text{ nm}$) pulses. The temperature of the STO substrate during the deposition was fixed at 690°C with an oxygen partial pressure of 20 mTorr and 100 mTorr for T-SRO and M-SRO thin films, respectively. Details on sample fabrication and characterization can be found in elsewhere.³³ *In situ* XRD

measurements were carried out at beamline 5D at Pohang Light Source in Korea. The X-ray energy was tuned to 10 keV by using a double bounce Si (111) monochromator. The thickness of T-SRO and M-SRO films estimated by the oscillation fringes period in the XRD pattern was approximately 40 nm. AP-XPS measurements were carried out at SOLEIL synchrotron (TEMPO beamline)⁴⁶ and PLS-II (8A2 beamline).⁴⁷ In the AP-XPS systems (PHOIBOS NAP 150, SPECS) consisting of the differential pumping scheme and advanced electrostatic lens design, it was possible to measure photoemission spectra up to the gas pressure of 25 Torr. Repeated cycles of oxygen annealing were carried out to achieve a clean surface of SRO films, i.e., annealing the sample at 120 °C for 15 min under an oxygen partial pressure of 10^{-6} Torr.

RESULTS AND DISCUSSION

Prior to XPS measurements, the crystal structure of the SRO thin film was confirmed by XRD. In Fig. 2(a), displaying the (002) specular reflection of T-SRO and M-SRO, the momentum transfer in the film normal z direction, q_z values of the T-SRO (red) peak are smaller than that of M-SRO (black) in reciprocal space, indicating that the lattice parameter of T-SRO along the c -axis is larger than that of M-SRO. The lattice parameters of T-SRO and M-SRO along the surface normal direction obtained from the (002) Bragg reflections are 3.969 Å and 3.952 Å, respectively, as shown in Fig. 2(b). The lattice parameters of T-SRO, M-SRO, and STO along the a -axis are all 3.905 Å due to compressive strain of the STO substrate exerted on the epitaxially stacked SRO thin film. The oscillatory patterns in Fig. 2(a) are thickness fringes originated from the interference between X-rays reflected from the substrate and thin film. The sharp fringes patterns indicate that the crystalline quality of the thin film sample was superb.⁴⁸

First, the XRD measurements of the off-specular $\langle 103 \rangle$, $\langle 013 \rangle$, $\langle \bar{1}03 \rangle$, and $\langle 0\bar{1}3 \rangle$ Bragg reflections were carried out at elevated

temperatures under UHV condition, as shown in Fig. 2(c). The sample temperature is indicated just below the spectra, e.g., room temperature RT (I), 150 °C (II), and 220 °C (III), for T-SRO and M-SRO. In Fig. 2(c), at RT and 150 °C, the q_z values of the M-SRO, $\langle 0\bar{1}3 \rangle$ and $\langle 013 \rangle$ peaks are different from the $\langle \bar{1}03 \rangle$ and $\langle 103 \rangle$ peaks, whereas T-SRO shows that q_z values of all $\{103\}$ plane family peaks are the same. In the off-specular geometry, the identical q_z values of all $\{103\}$ family peaks of the T-SRO film indicated the absence of octahedral tilting. On the other hand, in the case of M-SRO, the values of q_z of $\langle 103 \rangle$ and $\langle \bar{1}03 \rangle$ reflections are 4.756 \AA^{-1} and 4.780 \AA^{-1} , respectively. Previously, in M-SRO, having different q_z values in the off-specular geometry has been interpreted as the presence of octahedral tilting.³³ On the other hand, at 220 °C (III) (yellow shaded), all $\{103\}$ family peaks of M-SRO have the same q_z values, suggesting that octahedral tilting disappear. In short, the M-SRO undergoes SPT from the monoclinic to tetragonal phase near ~ 200 °C, whereas T-SRO shows no change under UHV. We note that the shift toward the lower q_z observed in all samples as temperature increases was due to the thermal expansion.

As mentioned previously, the role of oxygen vacancy becomes important as the phase transition takes place in the M-SRO thin film. To observe any surface modification due to the changes of oxygen vacancy at the onset of the phase transition, XPS measurements were carried out under the identical pressure and temperature conditions as used in Fig. 2. It is necessary to note that XRD provides bulk sensitive information, whereas XPS delivers surface sensitive information. Nevertheless, if there is any change of oxygen vacancy states at the bulk and interface of the SRO film, there is a possibility that the oxygen atoms out of the vacancies can migrate to the surface, resulting in the changes on surface chemical states.

Figure 3(a) shows the XPS spectra of Ru $3p$, Sr $3d$, and O $1s$ of T-SRO and M-SRO films obtained under UHV conditions from RT to 220 °C. The measurements were performed in the order of RT (I), 150 °C (II), 220 °C (III), and RT (IV). As shown in Fig. 3(a), no

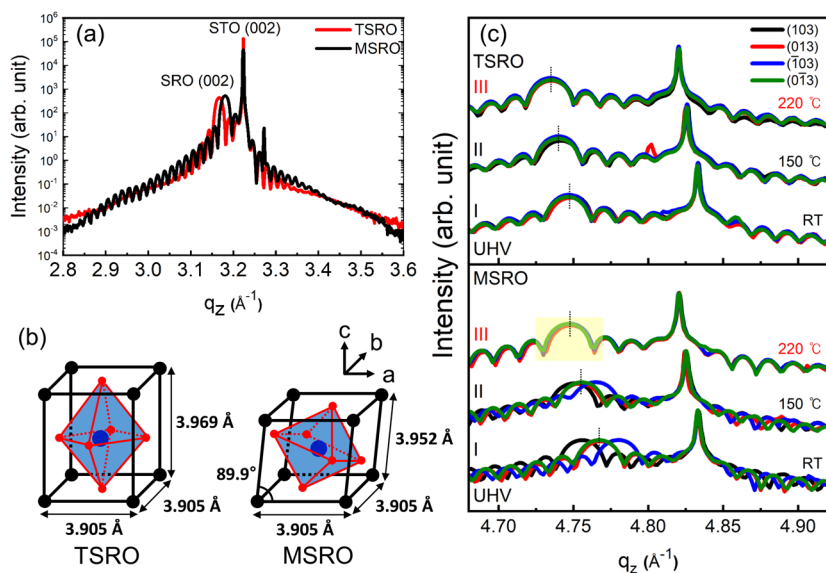


FIG. 2. (a) X-ray diffraction (XRD) measurement of T-SRO (red) and M-SRO (black) along the surface normal direction. (b) Schematic view of T-SRO (left) and M-SRO (right). The lattice parameters of T-SRO and M-SRO along the c -axis are 3.969 Å and 3.952 Å, respectively, and the lattice parameter of T-SRO and M-SRO along the a -axis is equal to 3.905 Å due to epitaxial strain by the STO substrate. (c) XRD measurements of T-SRO (top) and M-SRO (bottom) along the off-specular direction. Each black, red, blue, and green lines indicate the XRD results along the off-specular $\langle 103 \rangle$, $\langle 013 \rangle$, $\langle \bar{1}03 \rangle$, and $\langle 0\bar{1}3 \rangle$ directions, respectively. There are no changes found in T-SRO, but M-SRO shows that SPT occurs at 220 °C.

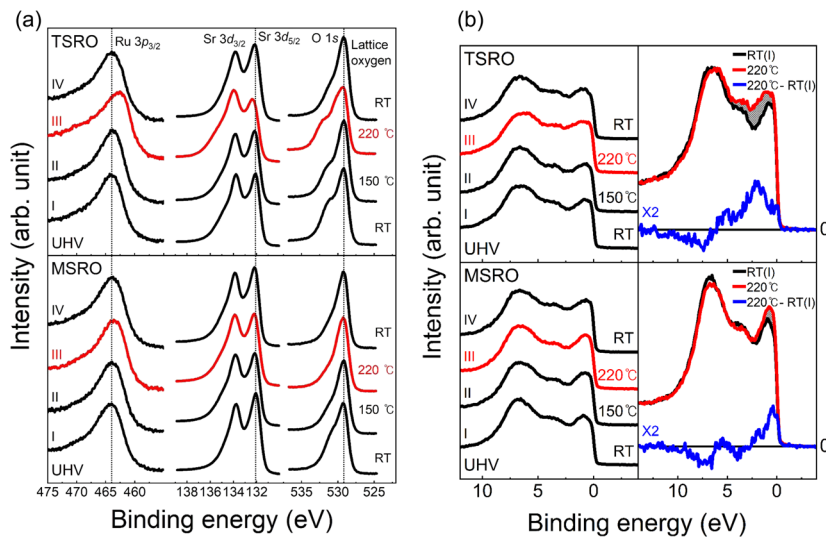


FIG. 3. (a) Core level XPS spectra of T-SRO (top) and M-SRO (bottom) under UHV conditions. (b) Valence band spectra of T-SRO (top) and M-SRO (bottom). Black (Red) lines indicate the results under UHV condition before (after) SPT. Blue lines indicate the difference between the valence band spectra of RT and 220 °C.

changes are found in the Ru 3p spectra in both T-SRO and M-SRO during I \rightarrow II step. On the other hand, as the temperature increases above the SPT temperature, ~ 220 °C, Ru 3p spectra of both films show the core level shift toward the lower binding energy direction. The binding energy of Ru 3p is shifted from 464.0 eV to 462.6 eV in T-SRO, and from 464.1 eV to 463.6 eV in M-SRO, respectively. The core level shift of Ru 3p can be interpreted as following. In SRO, Ru atoms share the electron with oxygen atoms in the SRO lattice. As mentioned previously, during the SPT, the presence of oxygen vacancy at the Sr-O plane is energetically more stable than the Ru-O plane.³⁷ Additionally, Ru atoms share less electrons with oxygen atoms along the z direction as oxygen vacancy is being generated. Also, the lattice along the z direction is being stretched during SPT, which changes the Coulomb interaction with neighboring oxygen atoms, can induce core level shift of Ru to lower binding energy direction.^{49,50} As the sign of oxygen vacancy starts to show near SPT temperature, it can be assumed that the origin of oxygen vacancies formed on surface is due to the strain release between STO and SRO across the SPT temperature.³⁷

In the case of Sr 3d spectra in Fig. 3(a), T-SRO and M-SRO show slightly different response to temperature than Ru 3p spectra. In the T-SRO film, the Sr 3d spectra show little change during I \rightarrow II step. Then, as temperature reaches 220 °C, the peak at higher binding energy side, ~ 133.5 eV, shows a significant increase. On the other hand, the M-SRO film shows similar, but smaller changes, as the T-SRO film is at temperature of 150 °C (I \rightarrow II) and remains unchanged at 220 °C. The M-SRO film returns to the original lineshape at RT, showing the reversibility during SPT. On the other hand, the lineshape after annealing is only slightly different from the lineshape at RT in the T-SRO film since only the M-SRO film shows SPT during the annealing process. According to the previous reports, the binding energies of Sr 3d_{5/2} in the SRO lattice and SrO_{1+x} oxide are ~ 132.0 eV and ~ 133.5 eV, respectively.⁵¹ That is, in both films, the spectral weight of the SrO_{1+x} oxide is increasing as the temperature increases. This observation can be possibly interpreted with the migration of oxygen atoms to the surfaces. As oxygen vacancy starts

to form near the SPT temperature, the oxygen inside the film starts to migrate and moves to the Sr-terminated surface, which is shown as the increased oxidation state of the Sr 3d spectra in Fig. 3(a). In other words, the spectral change of Sr 3d shows that the metastable Sr oxide layer is being formed on the surface through oxygen migration across the SPT temperature.^{50,51} The core level shift of the Sr 3d spectra toward the lower binding energy direction is negligible compared to Ru 3p spectra even if the oxygen vacancy is generated in the Sr-O plane. As the distance between Sr atoms and oxygen vacancy is much larger than that of Ru-O while the symmetric array of the Sr atoms is unchanged, the Coulomb potential that Sr experiences from the oxygen vacancy is much less than Ru. Additionally, the electronegativity of Sr is much lower than Ru.⁴⁹ The comparison of Sr 3d spectra between RT and T = 220 °C is shown in Fig. S1 of the [supplementary material](#), which clearly shows the presence of SrO_{1+x} oxide. It is important to note that the enhanced spectral contribution of oxides at T = 220 °C reduced to original when the temperature reduces to RT, i.e., a clear indication that oxygen comes from the inside of the films.

Since the number of oxygen vacancy is higher in the T-SRO film, the presence of migrating oxygen, i.e., surface SrO_{1+x} oxide, is more significant than M-SRO. In the case of the M-SRO film, the sign of oxygen vacancy exists from the increase in SrO_{1+x} oxide, yet the amount of surface oxide is not higher than T-SRO, resulting in the smaller increase in SrO_{1+x} oxide. As stated previously, the structure of the SRO thin film becomes tetragonal (monoclinic) below (above) 60 mTorr of oxygen partial pressure.³³ The T-SRO used in this experiment was fabricated at 20 mTorr of oxygen partial pressure, whereas M-SRO was fabricated at 100 mTorr of oxygen partial pressure. Thus, the oxygen vacancy concentration of T-SRO is much larger than the M-SRO, explaining the result of Sr 3d spectra.³⁵ In addition, as the oxygen in T-SRO can move easily due to larger oxygen vacancies, the peak shift of T-SRO becomes large when the same thermal energy is exerted on both T-SRO and M-SRO. The variation of surface SrO_{1+x} oxide and oxygen vacancy of Sr 3d spectra can be also found in O 1s spectra in Fig. 3(a). The amount of

oxygen in the bulk lattice reduces and Sr oxide increases as the SPT starts to take place in the film. Again, the change of oxygen spectra is more significant in T-SRO due to the higher density of oxygen vacancy. It is also noteworthy that the background of SrO_{1+x} oxide in T-SRO is increasing in the direction of higher binding energy. In other words, the core level shifts reflect the internal oxygen migration to surface across the SPT of the SRO thin film, and core level shifts of M-SRO are smaller than T-SRO since the concentration of oxygen vacancy in M-SRO is much lower than T-SRO. Also, as the temperature decreases to RT, the positions of the core level spectra are returned back to initial energies, indicating the reversibility of oxygen migration during the SPT of the SRO thin film.

In the discussion of Fig. 3, the possibility of surface oxygen vacancy formation due to the film decomposition under UHV annealing can be ruled out as SPT temperature (180–220 °C) is much lower than the temperature at which the SRO thin film is decomposed, i.e., the decomposition temperature of the SRO thin film is reported as high as 300 °C.⁵⁰ In the case of M-SRO, the concentration of oxygen vacancy is originally low. As the M-SRO film makes its transition from the monoclinic phase to tetragonal phase, the migration of oxygen atoms starts as early as 150 °C, showing the sign of SrO_{1+x} oxide. Yet, the amount of oxygen migration is relatively lower than T-SRO and the amount of SrO_{1+x} oxide is no longer increasing during SPT, which is due to the low amount of oxygen vacancy within the limited volume. In addition, the atomic ratios of Sr/Ru estimated from the XPS measurements remain constant during the SPT, indicating that no segregation of Sr or Ru occurs. Although there are reports on Ru deficiency contributing to the phase transition, no clear changes are found in the atomic ratio of Sr/Ru atoms.

The evidence of oxygen vacancy can further be found in the valence band spectra. In Fig. 3(b), the valence band spectra at each temperature and the comparison of the valence band spectra between RT and 220 °C are shown for both T-SRO and M-SRO films. In the case of the T-SRO film, the difference of the valence

band spectra between RT and 220 °C shows the sign of enhancement near the Fermi level and ~2.5 eV (blue line), which matches well with the oxygen vacancy features of density of states estimated from first-principle calculation in the previous report.³⁵ However, the difference of valence band spectra of the M-SRO film does not show much resemblance to that of T-SRO, which is possibly due to the lower concentration of the oxygen vacancy. It is consistent with the results of XPS core level spectra. The Ru 3*d* and Sr 3*p* spectra also exhibit an almost identical trend, as shown in Fig. S2. When the temperature is reduced back to room temperature, all the positions of XPS in M-SRO are back to the initial state, showing the reversibility of SPT. In the case of T-SRO, the lineshape of spectra is almost recovered during the annealing process with only slight difference. It is to be noted that this measurement was carried out under UHV, and no extra oxygen was being added to the film. This explains that the generated oxygen vacancy returns to the equilibrium position, and the structure is regained.

To check out the role of oxygen vacancy, the external source of oxygen was introduced by utilizing AP-XPS. Figures 4(a) and 4(b) show the Ru 3*p*, Sr 3*d*, O 1*s*, and valence band spectra under O₂ pressure of 100 mTorr at elevated temperatures. As shown in Fig. 4, the measurements of AP-XPS were conducted in the order of RT (V), 150 °C (VI), 220 °C (VII), and RT (VIII). The XPS spectra in Figs. 4(a) and 4(b) showed no visible changes during the SPT temperature. There is a small change in the Sr 3*d* in T-SRO film, but the amount of change is much smaller compared to the UHV condition. As the oxygen vacancy created during the SPT temperature has been filled up with the external oxygen source, the formation of surface SrO_{1+x} oxides is reduced significantly. Both T-SRO and M-SRO spectra VIII are almost identical to the spectra V, indicating annealing at 220 °C does not create additional surface oxide. On the other hand, the surface adsorbed oxygen was detected, which was different from that of Fig. 3 (UHV condition). In Fig. 4(a), the positions of the higher binding shoulder of O 1*s* and Ru 3*p* spectra at 220 °C are different from that of Fig. 3(a). In the case of O 1*s*, the shoulder position, i.e., the surface oxide peak, is located at higher

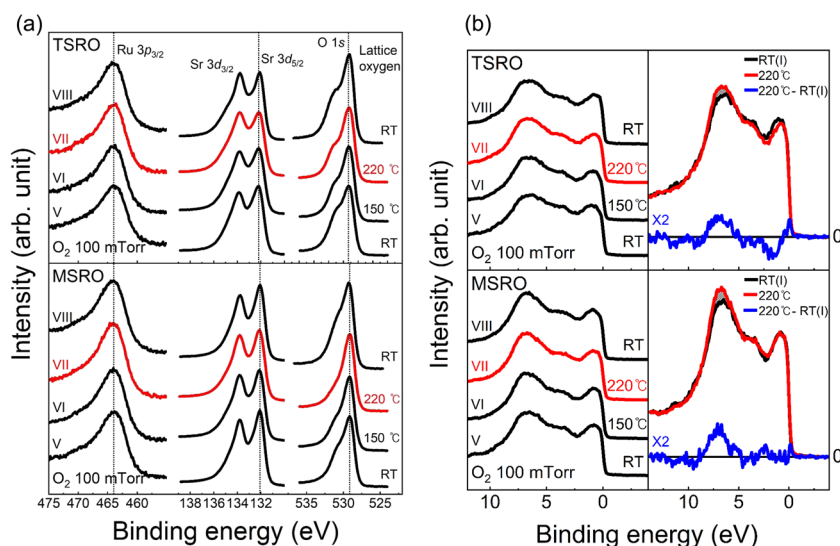


FIG. 4. (a) Core level XPS spectra of T-SRO (top) and M-SRO (bottom) under oxygen partial pressure of 100 mTorr. (b) Valence band spectra of T-SRO (top) and M-SRO (bottom) under oxygen partial pressure of 100 mTorr. Black (Red) lines indicate the results under UHV condition before (after) SPT.

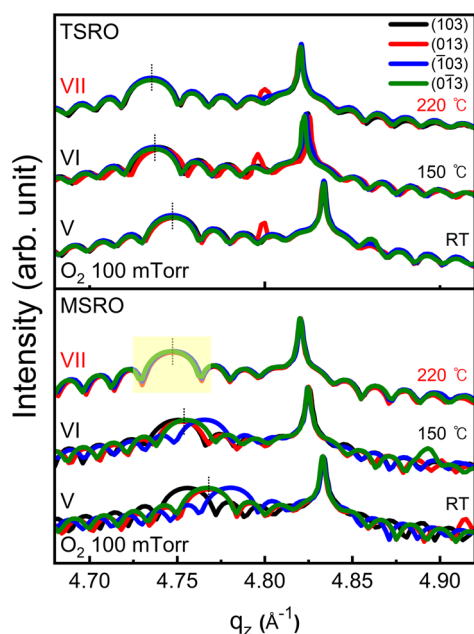


FIG. 5. XRD off-specular reflection elevated temperature under oxygen partial pressure of 100 mTorr. Each black, red, blue, and green lines indicate the off-specular direction along (103), (013), ($\bar{1}03$), and ($0\bar{1}3$), respectively. It shows the same trend as XRD off-specular reflection under UHV conditions, Fig. 2(c).

binding energy side, ~ 0.7 eV, than Fig. 3, which is the indication of a different origin of oxygen. The binding energy of the surface oxide peak under UHV is 531.7 eV, whereas 531.0 eV in the oxygen pressure environment, as shown in Fig. S3. The origin of the O 1s shoulder peak in Fig. 3(a) is due to the internal oxygen migration, whereas that in Fig. 4(a) originates from external gaseous oxygen. It is to note that the peak difference of M-SRO between UHV and oxygen pressure condition is not clearly visible due to the relatively lower concentration of oxygen vacancy than T-SRO.

To confirm if our observation in Figs. 2 and 3 is coming from the surface defect or the degradation of the sample, the SPT was checked again under oxygen condition. As shown in Fig. 5, we monitored the off-specular (103), (013), ($\bar{1}03$), and ($0\bar{1}3$) reflections of T-SRO and M-SRO films under 100 mTorr of oxygen pressure at elevated temperature. From the bottom, the measurements were performed in the order of RT (V), 150 °C (VI), and 220 °C (VII). As previously observed under the UHV conditions, M-SRO shows SPT at 220 °C, but T-SRO shows no change. That is, the SPT of the SRO thin film takes place regardless of the external gaseous pressure. The result of Fig. 5 confirms that the validity of samples and the observation of XPS measurements is mostly from the surface effect, indicating that the surface structure during SPT could be different from that of bulk properties.

CONCLUSION

In this paper, with *in situ* XRD and AP-XPS, we investigated the presence of oxygen vacancy of T-SRO and M-SRO films across

the SPT temperature. Across the SPT temperature, surface chemical shifts were observed in both T-SRO and M-SRO films, and the analysis of AP-XPS spectra suggested the sign of surface migration of lattice oxygen. In addition, the emerging valence band features during the SPT temperature showed good agreement with previously reported theoretical electronic structure calculations. Our finding suggests that there exists a close relation between oxygen vacancy and SPT. Our observation also suggests that bulk SPT of the SRO thin film can be possibly observed with XPS in an indirect manner. As a further study, the *in situ* surface XRD can be helpful for identifying surface structural changes during SPT.

SUPPLEMENTARY MATERIAL

See the [supplementary material](#) for comparison and analysis of core level photoemission spectra displaying surface oxide formation across structural phase transition on SRO thin films.

ACKNOWLEDGMENTS

This work was supported by the National Research Foundation of Korea (Grant Nos. NRF-2015R1A5A1009962, NRF-2017K1A3A7A09016316, NRF-2019R1A2C2008052, NRF-2017K1A3A7A09016395, and NRF-2019K1A3A1A21030984) and the GIST Research Institute Grant funded by the Gwangju Institute of Science and Technology (GIST) 2019. The Advanced Light Source is supported by the Office of Basic Energy Sciences of the U.S. DOE under Contract No. DE-AC02-05CH11231.

REFERENCES

- 1 C. Gu and J. S. Lee, *ACS Nano* **10**, 5413 (2016).
- 2 H. Nili, S. Walia, S. Balendhran, D. B. Strukov, M. Bhaskaran, and S. Sriram, *Adv. Funct. Mater.* **24**, 6741 (2014).
- 3 B. Hwang and J. S. Lee, *Sci. Rep.* **7**, 673 (2017).
- 4 D. Liu, Q. Lin, Z. Zang, M. Wang, P. Wangyang, X. Tang, M. Zhou, and W. Hu, *ACS Appl. Mater. Interfaces* **9**, 6171 (2017).
- 5 Z. Xiao, Y. Yuan, Y. Shao, Q. Wang, Q. Dong, C. Bi, P. Sharma, A. Gruverman, and J. Huang, *Nat. Mater.* **14**, 193 (2015).
- 6 A. R. Akbashev, L. Zhang, J. T. Mefford, J. Park, B. Butz, H. Luftman, W. C. Chueh, and A. Vojvodic, *Energy Environ. Sci.* **11**, 1762 (2018).
- 7 R. Mohamed, X. Cheng, E. Fabbri, P. Levecque, R. Kötz, O. Conrad, and T. J. Schmidt, *J. Electrochem. Soc.* **162**, F579 (2015).
- 8 J. Suntivich, K. J. May, H. A. Gasteiger, J. B. Goodenough, and Y. Shao-horn, *Science* **334**, 1383 (2011).
- 9 A. Vojvodic and J. K. Nørskov, *Science* **334**, 1355 (2011).
- 10 E. Fabbri, M. Nachtegaal, T. Binninger, X. Cheng, B. J. Kim, J. Durst, F. Bozza, T. Graule, R. Schäublin, L. Wiles, M. Pertoso, N. Danilovic, K. E. Ayers, and T. J. Schmidt, *Nat. Mater.* **16**, 925 (2017).
- 11 J. Luo, J. H. Im, M. T. Mayer, M. Schreier, M. K. Nazeeruddin, N. G. Park, S. D. Tilley, H. J. Fan, and M. Grätzel, *Science* **345**, 1593 (2014).
- 12 S. N. Tijare, M. V. Joshi, P. S. Padole, P. A. Mangrulkar, S. S. Rayalu, and N. K. Labhsetwar, *Int. J. Hydrogen Energy* **37**, 10451 (2012).
- 13 A. M. Glazer, *Acta Crystallogr., Sect. A* **31**, 756 (1975).
- 14 E. Pavarini and E. Koch, *Phys. Rev. Lett.* **104**, 086402 (2010).
- 15 R. E. Cohen, *Nature* **358**, 136 (1992).
- 16 J. He, A. Borisevich, S. V. Kalinin, S. J. Pennycook, and S. T. Pantelides, *Phys. Rev. Lett.* **105**, 227203 (2010).

- ¹⁷P. M. Woodward, *Acta Crystallogr., Sect. B* **53**, 32 (1997).
- ¹⁸J. M. Rondinelli and C. J. Fennie, *Adv. Mater.* **24**, 1961 (2012).
- ¹⁹I. Mazin and D. Singh, *Phys. Rev. B* **56**, 2556 (1997).
- ²⁰C. J. Howard and H. T. Stokes, *Acta Crystallogr., Sect. B* **54**, 782 (1998).
- ²¹P. M. Woodward, *Acta Crystallogr., Sect. B* **53**, 44 (1997).
- ²²C. B. Eom, R. J. Cava, R. M. Fleming, J. M. Phillips, R. B. Van Dover, J. H. Marshall, J. W. P. Hsu, J. J. Krajewski, and W. F. Peck, *Science* **258**, 1766 (1992).
- ²³P. B. Allen, H. Berger, O. Chauvet, L. Forro, T. Jarlborg, A. Junod, B. Revaz, and G. Santi, *Phys. Rev. B* **53**, 4393 (1996).
- ²⁴Y. Sugawara, K. Kamata, and T. Yamaguchi, *ACS Appl. Energy Mater.* **2**, 956 (2019).
- ²⁵B. J. Kim, D. F. Abbott, X. Cheng, E. Fabbri, M. Nachtegaal, F. Bozza, I. E. Castelli, D. Lebedev, R. Schäublin, C. Copéret, T. Graule, N. Marzari, and T. J. Schmidt, *ACS Catal.* **7**, 3245 (2017).
- ²⁶K. Wang, B. Zhang, W. Xie, S. Liu, X. Wei, Z. Cai, M. Gu, Y. Tao, T. Yang, C. Zhang, H. Cai, F. Zhang, and X. Wu, *ACS Appl. Nano Mater.* **2**, 3882 (2019).
- ²⁷D. G. Jeong, H. I. Ju, Y. G. Choi, C. J. Roh, S. Woo, W. S. Choi, and J. S. Lee, *Nanotechnology* **30**, 374001 (2019).
- ²⁸K. Y. Meng, A. S. Ahmed, M. Baćani, A. O. Mandru, X. Zhao, N. Bagués, B. D. Esser, J. Flores, D. W. McComb, H. J. Hug, and F. Yang, *Nano Lett.* **19**, 3169 (2019).
- ²⁹L. Si, O. Janson, G. Li, Z. Zhong, Z. Liao, G. Koster, and K. Held, *Phys. Rev. Lett.* **119**, 026402 (2017).
- ³⁰J. Matsuno, N. Ogawa, K. Yasuda, F. Kagawa, W. Koshibae, and N. Nagaosa, *Sci. Adv.* **2**, e1600304 (2016).
- ³¹Q. Qin, L. Liu, W. Lin, X. Shu, Q. Xie, Z. Lim, C. Li, S. He, G. M. Chow, and J. Chen, *Adv. Mater.* **31**, 1807008 (2019).
- ³²K. J. Choi, S. H. Baek, H. W. Jang, L. J. Belenky, M. Lyubchenko, and C. B. Eom, *Adv. Mater.* **22**, 759 (2010).
- ³³S. S. Lee, O. Seo, J. Kim, C. Song, S. Hiroi, Y. Chen, Y. Katsuya, and O. Sakata, *J. Korean Phys. Soc.* **73**, 1529 (2018).
- ³⁴S. H. Chang, Y. J. Chang, S. Y. Jang, D. W. Jeong, C. U. Jung, Y. J. Kim, J. S. Chung, and T. W. Noh, *Phys. Rev. B* **84**, 104101 (2011).
- ³⁵W. Lu, K. He, W. Song, C. J. Sun, G. M. Chow, and J. S. Chen, *J. Appl. Phys.* **113**, 17E125 (2013).
- ³⁶D. Kan and Y. Shimakawa, *Cryst. Growth Des.* **11**, 5483 (2011).
- ³⁷W. Lu, W. Dong Song, K. He, J. Chai, C. J. Sun, G. M. Chow, and J. S. Chen, *J. Appl. Phys.* **113**, 063901 (2013).
- ³⁸S. A. Lee, S. Oh, J. Lee, J. Y. Hwang, J. Kim, S. Park, J. S. Bae, T. E. Hong, S. Lee, S. W. Kim, W. N. Kang, and W. S. Choi, *Sci. Rep.* **7**, 11583 (2017).
- ³⁹S. A. Lee, S. Oh, J. Y. Hwang, M. Choi, C. Youn, J. W. Kim, S. H. Chang, S. Woo, J. S. Bae, S. Park, Y. M. Kim, S. Lee, T. Choi, S. W. Kim, and W. S. Choi, *Energy Environ. Sci.* **10**, 924 (2017).
- ⁴⁰H. T. Yi, B. Gao, W. Xie, S. W. Cheong, and V. Podzorov, *Sci. Rep.* **4**, 6604 (2014).
- ⁴¹W. Lu, P. Yang, W. D. Song, G. M. Chow, and J. S. Chen, *Phys. Rev. B* **88**, 214115 (2013).
- ⁴²X. Jiang, Y. Zhang, J. Jiang, Y. Rong, Y. Wang, Y. Wu, and C. Pan, *J. Phys. Chem. C* **116**, 22619 (2012).
- ⁴³Y. M. Kim, J. He, M. D. Biegalski, H. Ambaye, V. Lauter, H. M. Christen, S. T. Pantelides, S. J. Pennycook, S. V. Kalinin, and A. Y. Borisevich, *Nat. Mater.* **11**, 888 (2012).
- ⁴⁴G. Pacchioni, *ChemPhysChem* **4**, 1041 (2003).
- ⁴⁵H. Kim, J. Y. Zhang, S. Raghavan, and S. Stemmer, *Phys. Rev. X* **6**, 041063 (2016).
- ⁴⁶F. Polack, M. Silly, C. Chauvet, B. Lagarde, N. Bergeard, M. Izquierdo, O. Chubar, D. Krizmancic, M. Ribbens, J. P. Duval, C. Basset, S. Kubskey, and F. Sirotti, *AIP Conf. Proc.* **1234**, 185 (2010).
- ⁴⁷G. Kim, Y. Yu, H. Lim, B. Jeong, J. Lee, B. S. Mun, K. Kim, "AP-XPS beamline, a platform for operando science at Pohang Accelerator Laboratory," *J. Synchrotron Rad.* (in press) (2019).
- ⁴⁸D. Buttard, G. Dolino, D. Bellet, and T. Baumbach, *MRS Proc.* **452**, 437 (1997).
- ⁴⁹G. L. Yuan and A. Uedono, *Appl. Phys. Lett.* **94**, 132905 (2009).
- ⁵⁰J. Shin, S. V. Kalinin, H. N. Lee, H. M. Christen, R. G. Moore, E. W. Plummer, and A. P. Baddorf, *Surf. Sci.* **581**, 118 (2005).
- ⁵¹H. Schraknepper, C. Bäumer, R. Dittmann, and R. A. De Souza, *Phys. Chem. Chem. Phys.* **17**, 1060 (2015).